Oxidation inhibition of 3D printed porous steel by ceria-activated multilayers

Zhou, Zhipeng; Nadimpalli, Venkata Karthik; Lalwani, Aakil Raj; Wang, Shu; Shang, Yijing; Pan, Zhihao; Pedersen, David Bue; Esposito, Vincenzo

Published in:
Corrosion Science

Link to article, DOI:
10.1016/j.corsci.2023.111010

Publication date:
2023

Document Version
Publisher's PDF, also known as Version of record

Corrosion Science 214 (2023) 111010

Contents lists available at ScienceDirect

Corrosion Science

journal homepage: www.elsevier.com/locate/corsci

Oxidation inhibition of 3D printed porous steel by ceria-activated multilayers

Zhipeng Zhou [a,*], Venkata Karthik Nadimpalli [b], Aakil Raj Lalwani [b], Shu Wang [a], Yijing Shang [a], Zhihao Pan [b], David Bue Pedersen [b], Vincenzo Esposito [a,*]

[a] Department of Energy Conversion and Storage, Technical University of Denmark, 2800 Kgs Lyngby, Denmark
[b] Department of Civil and Mechanical Engineering, Technical University of Denmark, 2800 Kgs Lyngby, Denmark

ARTICLE INFO

Keywords:
Coating
Oxidation inhibition
Ceria
Laser powder bed fusion
Stainless steel

ABSTRACT

A 3D-printed porous 410 L steel support with a novel ceramic multi-coating is fabricated to improve the oxidation resistance of porous metal components for extreme conditions. Simplified support's morphology with straight channels fabricated by laser powder bed fusion enhances the applicability of wet-chemical coating methods. A multi-coating method combining electrophoretic deposition and infiltration improves the ceramic/steel interface. Ceria-based coatings with catalytic activity towards H_2O and O_2 provide both physical and dynamic chemical protection mechanisms. Excellent electro-chemo-mechanical stability and superior corrosion resistance (0.26 $\times 10^{-15}$ g^2 cm^4 s^{-1}) are shown at 750 °C in air-3 % H_2O for 122 h.

1. Introduction

The ceramic-metal joint is an efficient way to combine the mechanical resilience of metals with the hardness, electrical, chemical, and functional properties of certain ceramics. Electrochemical functional metal oxide coatings are especially used in harsh environments for high-temperature electrochemistry and catalysis [1]. This technology includes metal-supported solid oxide cells (MS-SOCs), energy conversion devices that work in particularly harsh thermos-chemical conditions. Typical operations are at temperatures above 600 °C in humid atmospheres. They convert a fuel's chemical energy efficiently into electricity (fuel cell mode, SOFC) or use electricity to produce fuel gases (electrolysis mode, SOEC) [2]. Compared with conventional ceramic SOCs, porous metal supports improved the robustness of MS-SOCs, allowing much faster startup and higher power density for wider applications [3,4]. However, the chemical instability of the interface between the metal support and the functional ceramics, such as metal oxidation/corrosion and element diffusion, limits the long-term stability of MS-SOCs [5].

Conventional porous metal supports by tape casting (one of the traditional powder metallurgy technologies) generally consist of sintered metal particles [6]. A schematic representation of the typical structure is shown in Fig. 1 (left). Metallurgical sintering necks link the metal particles, providing electronic conductivity and mechanical support [2]. As the sintered necks oxidize in the extreme working environment, the electrical conductivity decreases, resulting in a drastic performance degradation [5,6].

Coating methods, including dip-coating, infiltration, and electrophoretic deposition (EPD) with coating materials, such as spinels [7,8], perovskites [9–11], and other oxides containing rare earth elements [12–14], are used to form anti-oxidation layers to mitigate the corrosion issues of the metal. These methods allow the coating precursors (chemical solutions, suspension, or sol-gel) to fill the inner surface of the porous metal supports and form a protective interface after the reaction has taken place [7–15].

However, making a high-quality coating on the irregular inner surface of porous metal supports is challenging. The high-tortuosity channels of porous metal support formed by sintered powders can aggravate the segregation of the solution or colloid, challenging the uniformity of the coating/protective layer [7,9]. Decreasing the channels' tortuosity and geometrical complexity could be an effective way to improve coatings' applicability eventually. Laser powder bed fusion (LPBF), one of the standard laser-aided additive manufacturing (LAAM) technologies, is highly touted for making porous structures because of its almost unconstrained design freedom and precise forming for many alloys [16]. The porosity formed by LPBF is based on selective melting rather than sintering [17]. The porosity can be much easier to control in size and distribution, with the possibility of designing a 3D structure with low-tortuosity channels [18,19].

* Corresponding authors.
E-mail addresses: zhizho@dtu.dk (Z. Zhou), vies@dtu.dk (V. Esposito).

https://doi.org/10.1016/j.corsci.2023.111010
Received 7 December 2022; Received in revised form 20 January 2023; Accepted 23 January 2023
Available online 25 January 2023

Here, we propose a novel support design: low-Cr (12.5 %) ferritic stainless steel (410 L) supports with regularly distributed vertical straight gas channels. The supports are fabricated by LPBF 3D printing technology. This methodology allows a careful fabrication of the channels (Fig. 1, right), reducing the sintered-necks issue and tortuosity caused by metallic powders sintering (Fig. 1, left) [2,20], thus, enhancing gas diffusion and electrical conductivity of the support. Moreover, due to the simple geometry of the channels, the liquid, *e.g.* nanosuspension, will flow through the channels with high efficiency, allowing a uniform coating on the inner surface by wet-coatings methods.

Catalytically active materials are used as the coating, *i.e.* gadolinium-doped ceria and undoped ceria ($Ce_{0.9}Gd_{0.1}O_2$ and CeO_2). Ceria-based materials have a high chemical activity toward oxygen, hydrogen, steam, *etc*. [21–25]. Ceria also works as a chemical barrier, *i.e.*, a diffusion barrier layer (DBL), with the ability to inhibit elemental diffusion in SOCs [10,15,26,27]. The ceria-based coating is fabricated by a facile two-step approach that includes EPD of $Ce_{0.9}Gd_{0.1}O_2$ (CGO) nanoparticles, followed by infiltration with $Ce(NO_3)_3$. EPD obtains a uniform coating with nanopores, allowing $Ce(NO_3)_3$ solution to go through and contact the metal support surface. The uniform contact interface between the metal support and coating is achieved based on this liquid-solid reaction and the fast interdiffusion ability of the ceria with other oxides [28–31].

2. Experimental section

2.1. Metal supports fabrication

A home-built DTU open-architecture LPBF (Baxter) [32] equipped with an SPI laser, a ScanLabs IntelliScan Galvo, JenOptik F-θ lens, custom powder dosing, and wiper solutions integrated with a vacuum-tight chamber was used for metal supports fabrication. Brief manufacturing principles and main parameters are shown in Fig. 2a. The fabrication process was performed in nitrogen gas with an oxygen content lower than 200 ppm. A 410 L stainless steel powder (Höganäs Co.), with a nominal composition of Fe-12.5Cr-0.5Ni-0.5Si-0.03 C (wt. %) and a size range of 20–53 μm (Fig. 2b) were used for the processing. For the sample fabrication, porous cylinders 1.5 cm high and 1 cm in diameter (Fig. 2c) were fabricated at first. Finally, metal supports (Fig. 2d) were obtained by cutting cylinders into slices, grinding (400/800/1200/1500/2000 grit SiC sandpapers were used orderly), polishing (3 μm and 1 μm diamond compound polishing paste were used orderly), and cleaning in an ultrasonic bath.

2.2. EPD and infiltration

We fabricated the ceria-based coating by a two-step approach that includes EPD of $Ce_{0.9}Gd_{0.1}O_2$ (CGO) nanoparticles, followed by infiltration with $Ce(NO_3)_3$. The uniform protective layer was obtained by the reactions that occur during subsequent calcination and sintering.

The EPD suspension was prepared by mixing acetone (300 mL, purity-99 %), iodine particles (0.3 g, purity-99.8 %), and $Ce_{0.9}Gd_{0.1}O_2$ (7.5 g, specific surface area-12 $m^2\ g^{-1}$, Cerpotech Co.) with magnetic stirring and ultrasonic bath. After 16-h standing (precipitating the agglomerated particles), 200 mL were taken from the top of the suspension by a syringe for use in EPD. During the EPD coating, the iodine in the suspension reacted with acetone to form protons, as shown below [33,34]:

$$CH_3COCH_3 + 2I_2 \leftrightarrow ICH_2COCH_2I + 2H^+ + 2I^- \quad (1)$$

Positive charges were adsorbed onto the suspended CGO nanoparticles. The CGO nanoparticles were then deposited with an electric field (60 V/cm) onto the metal support that acted as the cathode (Fig. 3a). The deposition time for each sample was 3 min. After calcination, using 600 °C under argon flow for 4 h (600 °C/Ar/4 h), coated samples without infiltration were prepared (Non-Inf). An aqueous 1 M $Ce(NO_3)_3$ solution for infiltration was prepared by stirring $Ce(NO_3)_3{\cdot}6\ H_2O$ (Sigma-Aldrich Co., 99 %), Triton-X 100 surfactant (Talas Co.), and distilled water for 1 h. The Non-Inf samples were infiltrated with $Ce(NO_3)_3$ solution with the assistance of a vacuum pump. After the calcination with 600 °C/air/4 h, the infiltrated samples were named Inf.

2.3. Oxidation and electrochemical measurements

Platinum paste was painted on the top and bottom surfaces of coated samples as the current collector, followed by a treatment of 800 °C/air/4 h. Electrochemical impedance spectroscopy (EIS) was measured by Solartron 1260 at 750 °C in air-3 %H_2O with an amplitude of 15 mV and a frequency range of 0.06–30 MHz. The corrosion kinetics of samples were measured with cyclic oxidation experiments. Bare 410 L metal support, Non-Inf, and Inf samples after pre-oxidation (800°C/air/4 h) were aged at 750 °C in air-3 %H_2O with a total ageing time of 122 h using a tube furnace. Samples were taken out and weighed by a Sartorius balance with a resolution of 0.01 mg after 40, 80, and 122 h. The atmosphere of air-3 %H_2O was obtained by passing air through a bottle with water at room temperature.

2.4. Imaging and phase analysis

3D images were collected by a Nikon XTH 225 μfocus X-ray CT system. The voxel sizes are 7.97 μm (using 180 keV, 6.8 W) and 1.90 μm

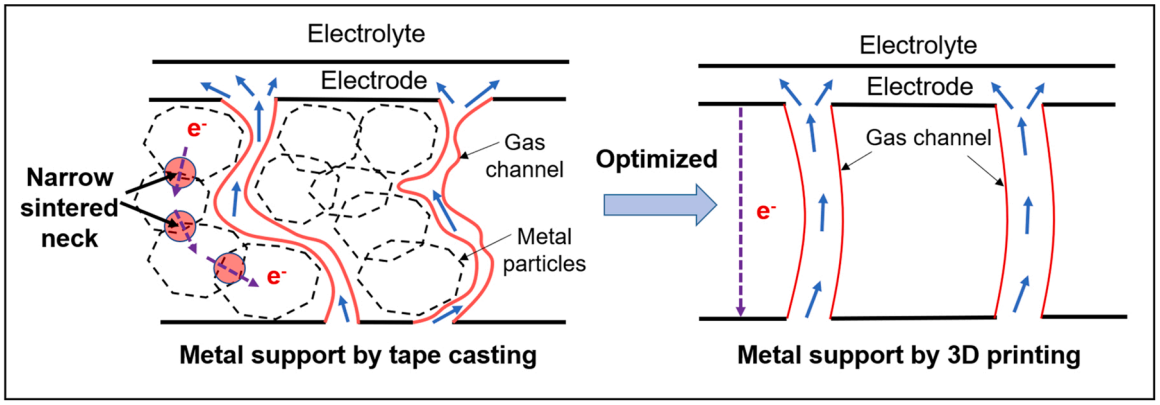

Fig. 1. Schematic diagram for optimizing metal support by 3D printing. (adapted from [2]).

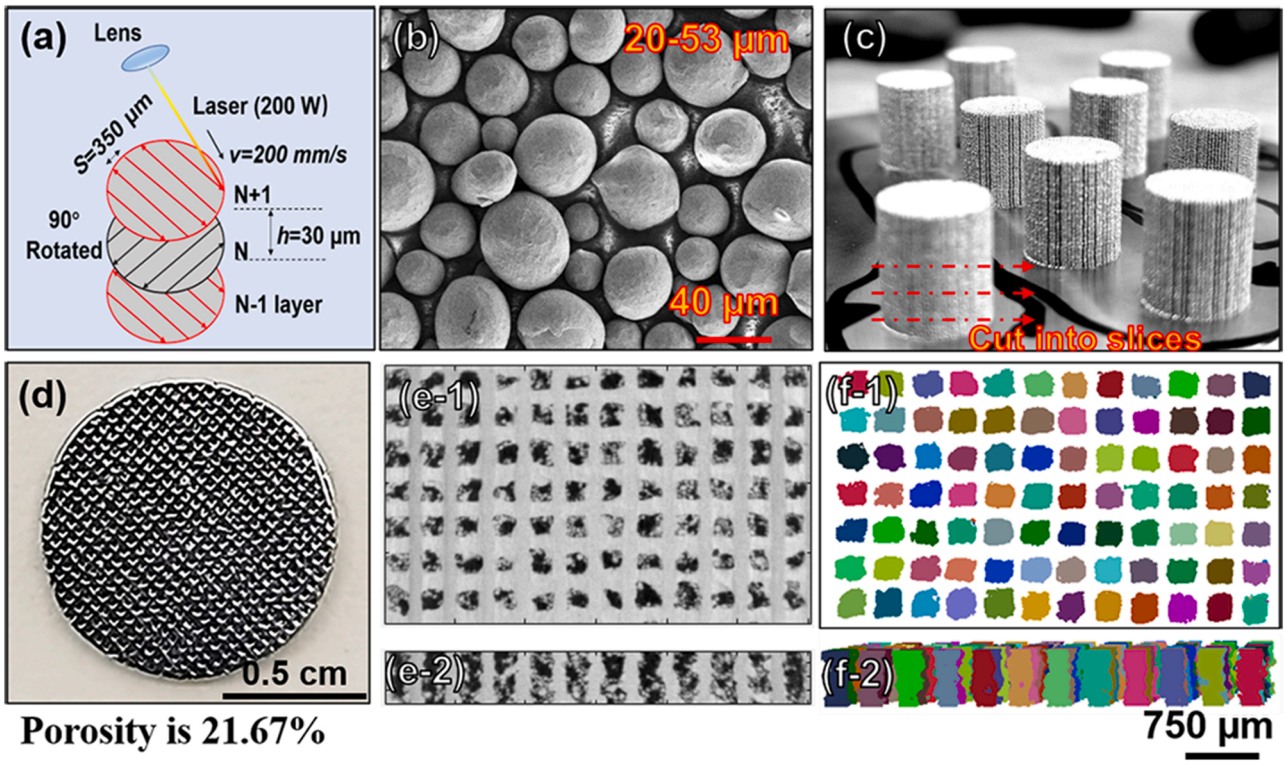

Fig. 2. Metal supports by LPBF. (a) Schematic diagram and process parameters of LPBF; (b) Morphology of 410 L powders prepared *via* argon gas atomization, with a diameter range of 25–50 μm; (c) Morphology of cylinders (1 cm in diameter and 1.5 cm in height) with straight vertical gas channels by LPBF; (d) Typical plan view of disk sample cut from cylinders in (c); (e) Reconstructed X-ray computed tomography (CT) images of (d) in plan view (e-1) and cross-section view (e-2); (f) Data analysis results by MATLAB corresponding to (e), the colour blocks represent gas channels.

(220 keV, 2.9 W) for the bare metal support (Fig. 2) and aged multi-coated metal support (Fig. 10), respectively. Here, to obtain the high resolution of X-ray tomography images, a piece with around 1.2 × 1.0 × 0.5 mm cut from the aged multi-coated sample was used for the X-ray detection. The Nikon CTpro3D software was used for the reconstruction. A MATLAB script and commercial software Avizo 9.4 were used to analyze samples' porosity and surface area (only interconnected porosity/surface were counted). The microstructure and morphology of the coating were characterized using a Leica optical microscope (OM) and a Zeiss Ultra scanning electron microscope (SEM) with an energy-dispersive (EDS) detector. An accelerating voltage of 15 keV and a working distance of 8 mm was used for SEM and EDS. Phase identification was performed using an Aeris X-ray diffractometer (XRD) with Cu Kα radiation, a scanning rate of 5°/min, a step size of 0.01°, and a range of 15–85°.

3. Results and discussion

3.1. Fabrication and Characterization

The LPBF method directly prints metallic shapes from a powder bed/metal substrate. The starting metallic powders undergo local heating with melting and solidification depending on the fluence of the input laser energy [35]. Cylinders (Fig. 2c) with straight vertical gas channels were fabricated by LPBF (Fig. 2a) with 410 L stainless steel spherical powders (Fig. 2b). The metal support slices (~ 0.5 mm thick) were obtained by cutting the cylinders and grinding and polishing (Fig. 2d). Fig. 2e shows the metal support structure in the plan view (Figs. 2e-1) and the cross-section view (Figs. 2e-2) by reconstructing the X-ray computed tomography data. Fig. 2 f shows the interconnected porosity distribution corresponding to Fig. 2e, with different colours for each gas channel, making up about 21.67 % of the total volume. The specific surface area is about 38.27 cm^2 g^{-1}.

The coating for the metal supports is obtained by a two-step process. Firstly, the metal supports were coated with CGO nanoparticles by EPD (Fig. 3a). Then, after 4 h calcination at 600 °C in argon, a uniform white coating forms on the metal surface (Fig. 3b). Fig. 3c shows the CGO coating with nano porosity covering the channels' surface. For the second step (Fig. 4), the nanoporous structure is thoroughly infiltrated with $Ce(NO_3)_3$ solution. After the calcination (600 °C/air/4 h) and the pre-oxidation (800 °C/air/4 h), a homogeneous oxide layer interface with uniform elemental distribution is obtained (Fig. 4c and e).

The oxide layer begins forming during calcination for samples infiltrated with $Ce(NO_3)_3$ solution (Inf samples). The decomposition of $Ce(NO_3)_3$ includes a highly diffusive step, forming a uniform mixed metal oxide layer on the steel surface (Fig. 4e) [36]. Therefore, a more uniform interface between the coating and the steel is shown in the Inf sample (see Fig. 4b and c for comparison). Meanwhile, as the products of the decomposition of $Ce(NO_3)_3$, CeO_2 particles fill the nano porosity of the CGO coating and make the coating more uniform and compact.

3.2. Electrochemical and chemical stability

The coated samples were tested in humid air (3 % vol H_2O) at 750 °C to speed up the oxidation [37]. The oxidation of the steel support is accompanied by elemental diffusion/migration at the ceramic/steel interface, which changes the total resistance of the system constituted by the steel support, ceramic/steel interface, and ceramic coatings. The electrochemistry and chemical stability of this system can be evaluated by the stability of the sample's area-specific resistance (ASR) using the ohmic component of the impedance (Z_{real}) [38,39]. The schematic diagram in Fig. 5 shows the oxidation at 750 °C in air-3 % H_2O for 122 h. The low-frequency range from 0.06 to 15 Hz describes the resistance of coated samples [39,40], and the Z_{real} value measured at the minimum frequency of 0.06 Hz fairly represents the real ohm resistance of samples. The Bode plots in Fig. 5a and b are for the Non-Inf sample when

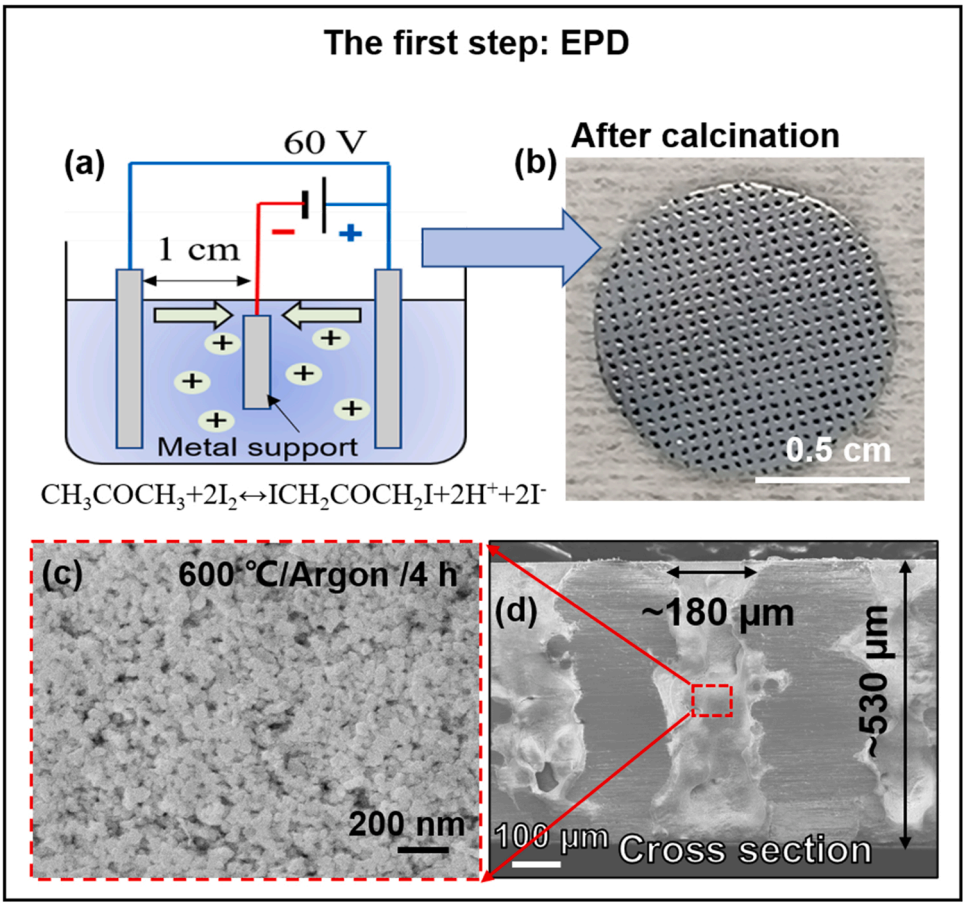

Fig. 3. Nano CGO coating by EPD. (a) Schematic diagram of EPD; (b) Typical coated sample after calcination (600 °C/Ar//4 h); (c) Microstructure of the coating located at the surface of the gas channel; (d) Cross-section of the coated sample.

t = 0 h and t = 122 h, and Fig. 5d and e are for the Inf sample. The results indicate that Z_{real} values of Non-Inf and Inf samples are stable in the low-frequency range of 0.06–1 Hz. ASR is plotted against ageing time in Fig. 5c for the Non-Inf sample and in Fig. 5f for the Inf sample.

Notably, for the Non-Inf sample, a decrease of about 36 % in ASR is shown after 122 h ageing (Fig. 5a *vs* 5b). A rapid decrease of ASR with a rate of *ca.* 15 Ω cm^2 h^{-1} was observed at the beginning of the test. The rate of decrease then remains stable at around 2 Ω cm^2 h^{-1} after 80 h (Fig. 5c). An overall decrease of *ca.* 9 % is registered for the Inf sample (Fig. 5d *vs* 5e). A slight ASR decrease with a rate of about 0.16 Ω cm^2 h^{-1} is shown within the first 10 h of the test. Then the ASR remains almost stable at around 38 Ω cm^2 with no further decrease. A large difference in ASR values level between Non-Inf and Inf samples is shown (Fig. 5c *vs* f), which should be ascribed to the increased CeO_2 and coating density.

Phase and elemental analyses were carried out on the prepared (t = 0 h) and post-mortem (t = 122 h) samples to analyze the results of the corrosion tests. XRD spectra are shown in Fig. 6. Before the ageing (t = 0 h), only peaks of Fe-Cr and CGO were detected in both Non-Inf and Inf samples. Then Fe-Cr-Mn oxide peaks (containing Fe, Cr, or Mn) appeared after the 122-h ageing. The specific oxides' phases are shown in Fig. 6b-d. $(Fe_{0.6}Cr_{0.4})_2O_3$ phase is detected in both Non-Inf and Inf samples (Fig. 8d), which should be the inner-layer oxides $(Fe_{1-x}Cr_x)_2O_3$ that were formed at high temperatures in the air [41]. Compared with the Inf sample at t = 122 h, Fe_3O_4 is detected in the Non-Inf sample (Fig. 6b). Fe_3O_4 is an expected corrosion product in humid air at high temperatures [42]. The possible presence of spinel oxides $MnCr_2O_4$ and $FeCr_2O_4$ was revealed in both the Inf and Non-Inf samples (Fig. 6 c), and spinel phases $Mn_{1-x}Fe_xCr_2O_4$ ($0 \leq x \leq 1$) are expected..

These spinels are reported to inhibit the thickening of the oxide layer by suppressing the outward migration of metal ions [7,43,44]. The stronger intensity of the XRD peaks shown in Fig. 6c and d suggest a thicker oxide layer in the Non-Inf sample than in the Inf sample. It is worth mentioning that Fe-Cr relative peak intensity decreases in the Inf sample compared with the Non-Inf sample (see the yellow region in Fig. 6a), which can be ascribed to the increased CeO_2 in the coating after the infiltration. Besides the phase identification by XRD, SEM and EDS give direct evidence of the oxidation results.

Fig. 7 shows the microstructure and elemental distribution of Non-Inf and Inf samples before and after ageing. Compared with the Non-Inf samples, less porosity is observed in the Inf samples (Fig. 7b *vs* a, Fig. 7d *vs* c), indicating a denser coating for the Inf samples. A detailed description of the chemical composition of the active DBL in the Inf sample after ageing is also reported in Fig. 8.

More severe corrosion appeared in the Non-Inf sample after ageing. An oxide layer of *ca.* ~1 μm thick appeared in the Non-Inf sample, while it was *ca.* 0.2 μm for the Inf sample (Fig. 7c *vs* 7d). Moreover, compared with the Non-Inf sample, the Inf sample formed a more uniform protective layer, including the thin oxide layer and active diffusion barrier layer (DBL). According to EDS line scanning profiles (Fig. 7e-f), steel elements show a dramatic decrease at the active DBL region. These results are attributed to the ability of CGO and CeO_2 to inhibit elemental interdiffusion by trapping the elements in the reaction products. This effect is highly desirable in SOCs as it prevents electrodes from elemental poisoning through the electrode/electrolyte and electrode/metal support interface [10,15,26,27].

The reaction and interdiffusion between steel's oxides and ceria-based coatings are expected to occur. Taking the reaction between

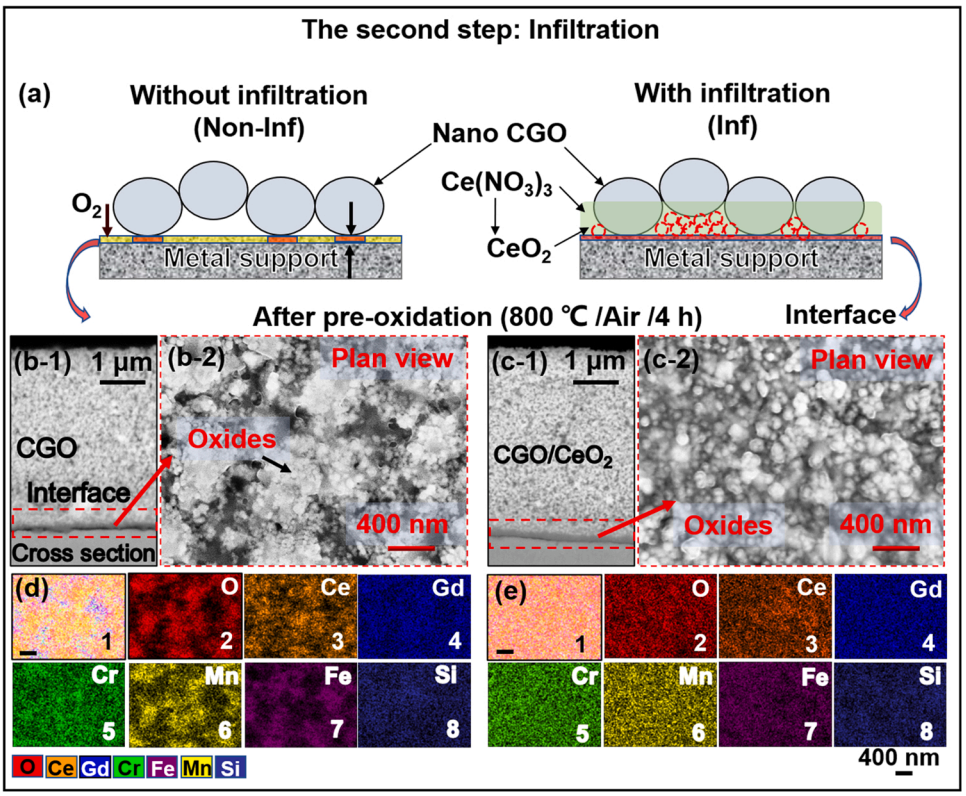

Fig. 4. Multi-coatings with the improved interface by Infiltration. (a) The coating without infiltration (Non-Inf) *versus* with infiltration (Inf); (b-1) Microstructure of Non-Inf sample in cross-section view; (b-2) Plan view of the polished interface between the coating and the metal support; (c) Microstructure of the Inf sample in cross-section view (c-1) and its polished interface in plan view (c-2); (d) EDS mappings corresponding to (b-2), where (d-1) is the superposition of (d-2)-(d-8); (i) EDS mappings for (c-2), where (e-1) is the superposition of (e-2)-(e-8).

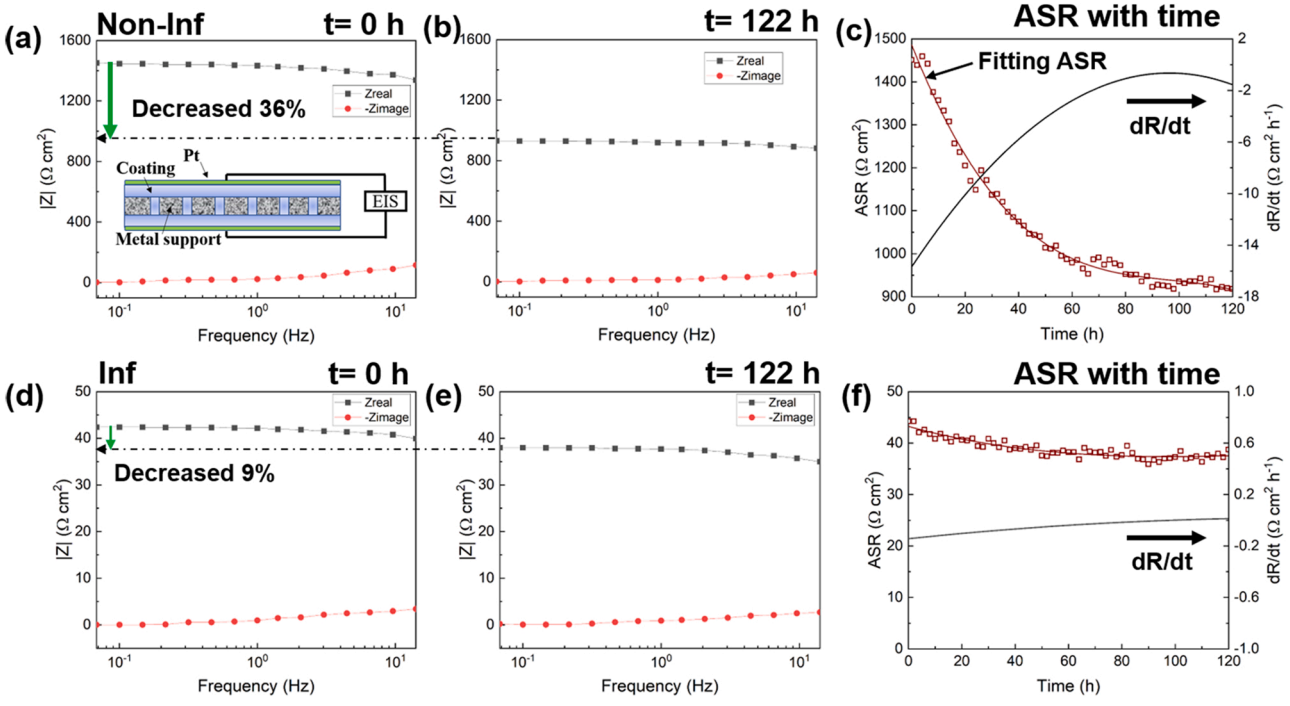

Fig. 5. EIS and ASR at 750 °C in Air-3 % H_2O for 122 h. (a) and (b) are Bode plots (0.06–15 Hz) of Non-Inf sample when t = 0 h and t = 122 h, respectively; (c) The relationship between ASR and time of Non-Inf sample; (d) and (e) are Bode plots of Inf sample when t = 0 h and t = 122 h, respectively; (f) The relationship between ASR and time of Inf sample, note the ASR curve was obtained by fitting with a cubic polynomial, and the ASR increasing rate was represented by dR/dt.

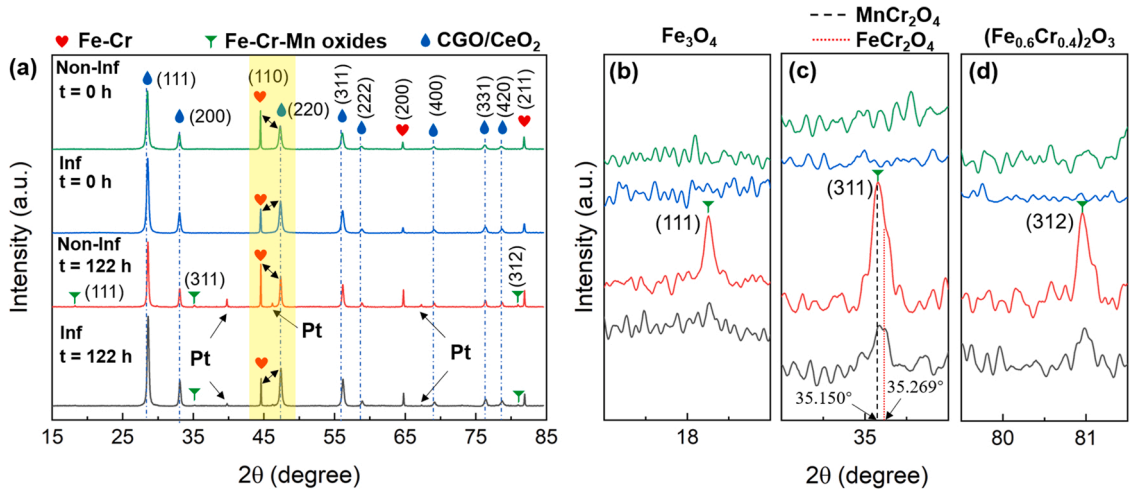

Fig. 6. (a) XRD spectra of coated samples with the status of t = 0 h and t = 122 h; (b), (c), and (d) are enlargements of (a) with the 2Θ range of 17° – 19°, 34° – 36°, and 79.5° – 81.5°, respectively. The XRD patterns are normalized to the maximum intensity.

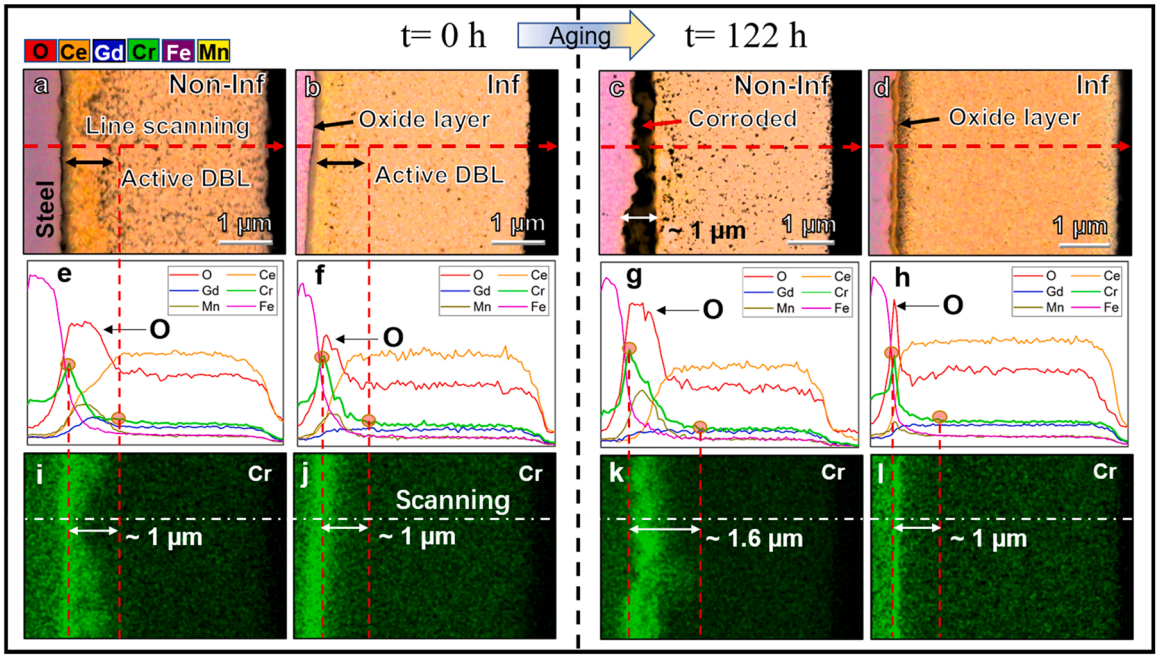

Fig. 7. Cross-sectional elements' distribution of coated samples with the status of t = 0 h and t = 122 h. Figs. (a)-(d) are superimposed images by backscattered electron images (BSE) and EDS mappings of Non-Inf and Inf; (e)-(h) are EDS line scanning profiles corresponding to (a)-(d), respectively; (i)-(l) are EDS mappings shown the distribution of Cr corresponding to (a)-(d), respectively. DBL stands for the diffusion barrier layer.

CeO_2 and Cr_2O_3 as a representative example [45,46]:

$$Cr_2O_3 = 2Cr_i^{\cdots} + \frac{3}{2}O_2 + 6e' \quad (2)$$

$$CeO_2 + Cr_i^{\cdots} = Ce_{Cr}^{\cdot} + Cr_{Cr} + V_o^{\cdot\cdot} + 2O_O \quad (3)$$

$$Ce_{Cr}^{\cdot} + Cr_{Cr} + 3O_O = CeCrO_3 + h^{\cdot} \quad (4)$$

The concentration of interstitial Cr defects decreases due to the substitution of Ce in the Cr lattice, inhibiting the growth/diffusion of Cr. Meanwhile, oxygen vacancies formed in doped-ceria and undoped under these conditions are expected to inhibit further cations' outward migration [13,45,46]. Chalphad calculation indicates that $CeCrO_3$ could be stable in the air below 800 °C (see Fig. S1 and ref. [47]). Other perovskites with a similar composition as $CeCrO_3$ are often reported in steel oxidation as $REMO_3$ phases; they are formed by the reaction between rare earth (RE is primarily Ce, Gd, La, Sm, and Y) oxide and metal (M is Fe, Cr, and Mn) oxides of the steel [13,48–51].

Although XRD cannot directly identify $REMO_3$ phases in our samples, the elemental analysis indicated that the ceria-coating reacting with steel elements produces the active DBL. It resulted in more effectiveness as the denser. Taking the Cr diffusive path in Fig. 7e and f as a reference, the active DBL was already formed in both Non-Inf and Inf samples (Fig. 7a and b) before the ageing with similar thicknesses. Following the Cr profile, a homogeneous active DBL is shown in the Inf sample. Fast diffusion provided by the infiltration facilitated the formation of a uniform Cr-containing oxide film during the calcination [7]. Meanwhile, the porosity in the coating was filled by CeO_2 nanoparticles, providing a more uniform contact interface with the steel and denser coating. As a result, the improved steel/ceramic interface and protective

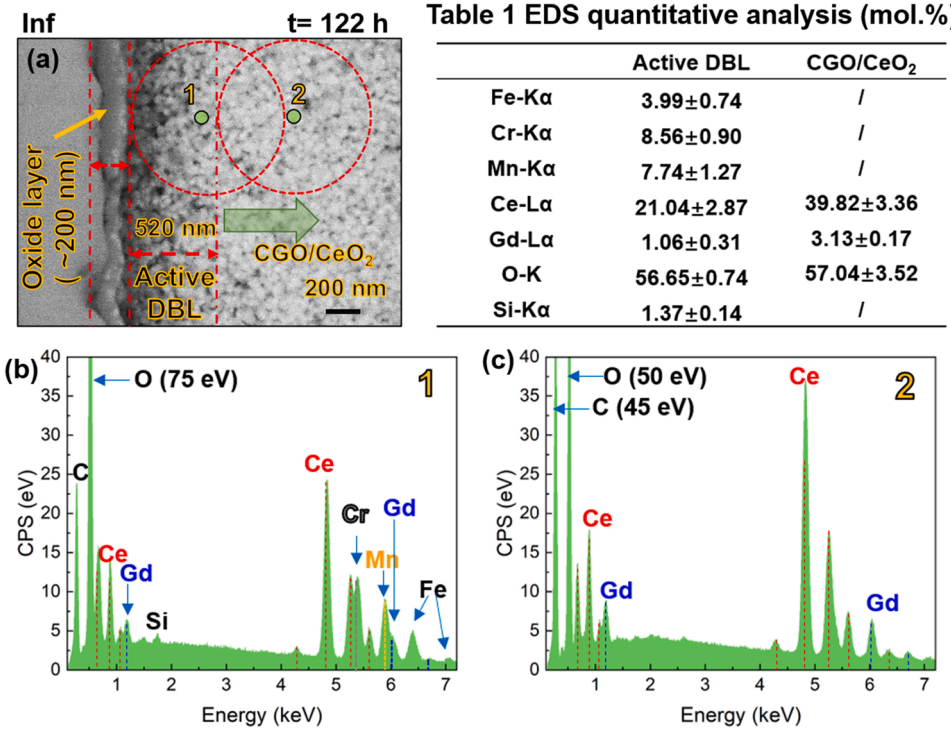

Table 1 EDS quantitative analysis (mol.%).

	Active DBL	CGO/CeO_2
Fe-Kα	3.99±0.74	/
Cr-Kα	8.56±0.90	/
Mn-Kα	7.74±1.27	/
Ce-Lα	21.04±2.87	39.82±3.36
Gd-Lα	1.06±0.31	3.13±0.17
O-K	56.65±0.74	57.04±3.52
Si-Kα	1.37±0.14	/

Fig. 8. EDS quantitative analysis of sample Inf with the status of t = 122 h. (a) Cross-sectional BSE image corresponding to Fig. 7d; (b) and (c) EDS spectra of points 1 and 2 in (a).

layer lead to uniform elemental diffusion during the pre-oxidation (Fig. 7a *vs* 7b) and ageing process (Fig. 7c *vs* 7d).

After 122 h of the test, Cr migrated about 0.6 μm into the ceramic coating for the Non-Inf sample (Fig. 7i *vs* 7k), while there was almost no change for the Inf sample (Fig. 7j *vs* 7 l). The Cr migration in the Non-Inf sample could be caused by Cr evaporation. The volatile Cr vapour species such as CrO_3, $CrO_2(OH)_2$, and CrO(OH) could be formed when Cr oxides are exposed to the humid air at high temperatures [52]. No obvious Cr evaporation appeared in the Inf sample, indicating that the contact of the oxide layer with the humid air was limited. This effect is attributed to the dense CGO/CeO_2 coating and its chemical activity toward O_2 and H_2O at high temperatures (detailed discussion, see Section 3.3).

A detailed representation of the compositions of the Inf-sample after ageing is revealed by EDS quantitative analysis (Fig. 8). A comprehensive analysis of the chemical composition was carried out to track the dilutions on the steel elements across the ceria-based coatings. The real active DBL in Fig. 8 was further distinguished from the ceria-based coatings (no steel elements were detected). Furthermore, the electron beam interactions [53] with steel elements were taken into account, *i.e.*, the red dotted circles surrounding points 1, and 2 represent the interaction zone of EDS for Cr, Mn, and Fe (see S2 in Supporting information for details of the calculation).

Point 2 is selected as the position closest to the active DBL without steel elements (Fig. 8c). Five points in CGO/CeO_2 region were also measured by EDS at the same distance from the steel surface. They consistently give similar values, which were averaged and reported in Table 1. The mole ratio of Ce/Gd in the CGO/CeO_2 region is about 12.7, *i.e.*, higher than that of $Ce_{0.9}Gd_{0.1}O_2$ (~9.2 of EDS detection result), which is caused by the infiltrated CeO_2.

Point 1 is selected in the active DBL closer to the steel/coatings interface. Five points along the boundary were also measured by EDS and averaged (Table 1). These values show a typical EDS profile as in Fig. 8b. Strong peaks of steel elements, especially Cr and Mn, were detected in the EDS spectrum (Fig. 8b), indicating the intense elemental diffusion occurring in the active DBL. Besides $CeCrO_3$, Mn- and Fe-riched perovskite compounds $REMO_3$ could also be formed during the solid-state elemental diffusion and reactions [54,55]. However, once the uniformly-distributed $REMO_3$ phases are formed, the elemental diffusion is inhibited, and the further increase of $REMO_3$ phases is slow. Therefore, as also reported in refs. [47,56], XRD cannot directly detect $REMO_3$ phases due to their small amount (Fig. 6). Although the existence of $REMO_3$ phases is not confirmed experimentally here, Chalphad calculation results (Fig. S1) and the DBL working mechanism [6,10,13] of CGO/CeO_2 suggest their formation.

Table 1
EDS quantitative analysis (mol. %).

	Active DBL	CGO/CeO_2
Fe-Kα	3.99 ± 0.74	/
Cr-Kα	8.56 ± 0.90	/
Mn-Kα	7.74 ± 1.27	/
Ce-Lα	21.04 ± 2.87	39.82 ± 3.36
Gd-Lα	1.06 ± 0.31	3.13 ± 0.17
O-K	56.65 ± 0.74	57.04 ± 3.52
Si-Kα	1.37 ± 0.14	/

3.3. Mechanisms and 3D structure stabilization

No Fe_3O_4 and Cr evaporation was detected or observed in Inf samples indicating that the multi-coatings effectively limit the contact between the humid air and the steel support. This effect cannot be completely attributed to the physical isolation effect of the coatings since the $Ce_{0.9}Gd_{0.1}O_2$/CeO_2 coatings cannot be fully dense at this low sintering temperature (800 °C). Therefore, the effect can be attributed to the chemical reactivity of cerium oxide to the humid air.

CeO_2 is usually regarded as oxygen-defective oxides CeO_{2-x} ($0 < x < 0.5$), with both Ce^{3+} and Ce^{4+} oxidation states. During ageing, the reaction cycles between CeO_{2-x} and the humid air should be considered [57,58]:

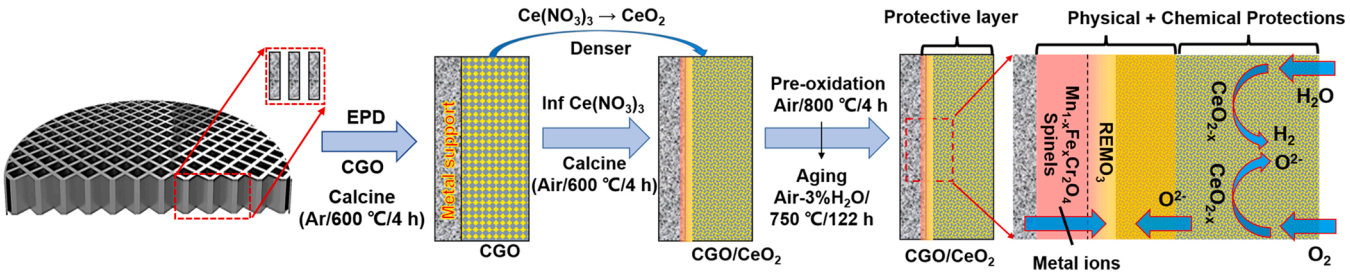

Fig. 9. Schematic of the coating process and oxidation inhibition mechanism.

$$CeO_{2-x}+\frac{x}{2}O_2 \rightarrow Ce^{4+}+2O^{-2} \quad (5)$$

$$CeO_{2-x}+\frac{x}{2}H_2O \leftrightharpoons CeO_2+\frac{x}{2}H_2 \quad (6)$$

$$H_2+O^{-2} \rightarrow H_2O \quad (7)$$

As a result of such reaction cycles and the slow gas diffusion caused by the relatively dense CGO/CeO_2 coating with catalytic activity, the humid air would be limited to contact with the oxide layer, suppressing the oxygen activity at the steel/coating interface.

On the other hand, $Mn_{1-x}Fe_xCr_2O_4$, and the possible presence of $REMO_3$ oxides concentrate at the steel/ceramic interface, inhibiting the outward migration of metal ions. The mechanism is schematically represented in Fig. 9. These chemical and physical protection mechanisms improve the corrosion resistance of metal supports.

It is worth mentioning that the protection mechanisms discussed above should exist in both Non-Inf and Inf samples as both contain CeO_2 (CGO is Gd-doped CeO_2, which contains CeO_2). The better protection effects of Inf samples should be attributed to the more contained CeO_2 and higher density of coatings. The high-density coating will slow gas diffusion, and highly contained CeO_2 in the coating enhances the humid air's catalytic effect, facilitating the reaction cycles (Eqs. 5–7).

Fig. 10 gives the final evaluations of multi-coated samples on matching, coverage, and corrosion kinetics. Although chemical expansion and fast interdiffusion are expected in ceria by redox reactions [21, 28,29,58], all the samples show excellent electro-chemo-mechanical stability in the thermochemical process. After 122-h ageing, the coating still matches the steel support, even in the region with a high-tortuosity surface (Fig. 10a). Continuous coatings cover all inner surfaces. A 3D distribution of coatings is obtained by X-ray computed tomography, as shown in Fig. 10b. The oxidation mass gain of metal support is effectively inhibited by this high-quality and stable coating. Superior oxidation resistance is shown according to the evaluation results of corrosion kinetics (Fig. 10c and d).

The evaluations of corrosion kinetics from corrosion resistance according to two equations are shown in Fig. 10c and d. The first equation uses the oxidation weight gain per unit area, as shown below [59,60]:

$$\left(\frac{\triangle m}{A}\right)^2 = K_P t + C \quad (5)$$

where $\triangle m$ is the measured mass change (g), A is the surface area of the substrate (cm^2), K_P is the parabolic rate constant ($g^2\ cm^{-4}\ s^{-1}$), t is the ageing time (s), and C is an integration constant defining the onset of parabolic kinetics. Here, the value of K_P depends on the surface area measurement's accuracy. Therefore, for the porous metal supports with indeterminate morphology, a second equation non-including the effects of the surface area is used, as shown below [38]:

$$\left(\frac{\triangle m}{m}\right)^2 = K'_P t[\%^2] \quad (6)$$

where m is the initial mass (g), and K'_P is the parabolic rate constant ($\%^2\ h^{-1}$). Eq. (5) gives the more physical result, while Eq. (6) gives the result

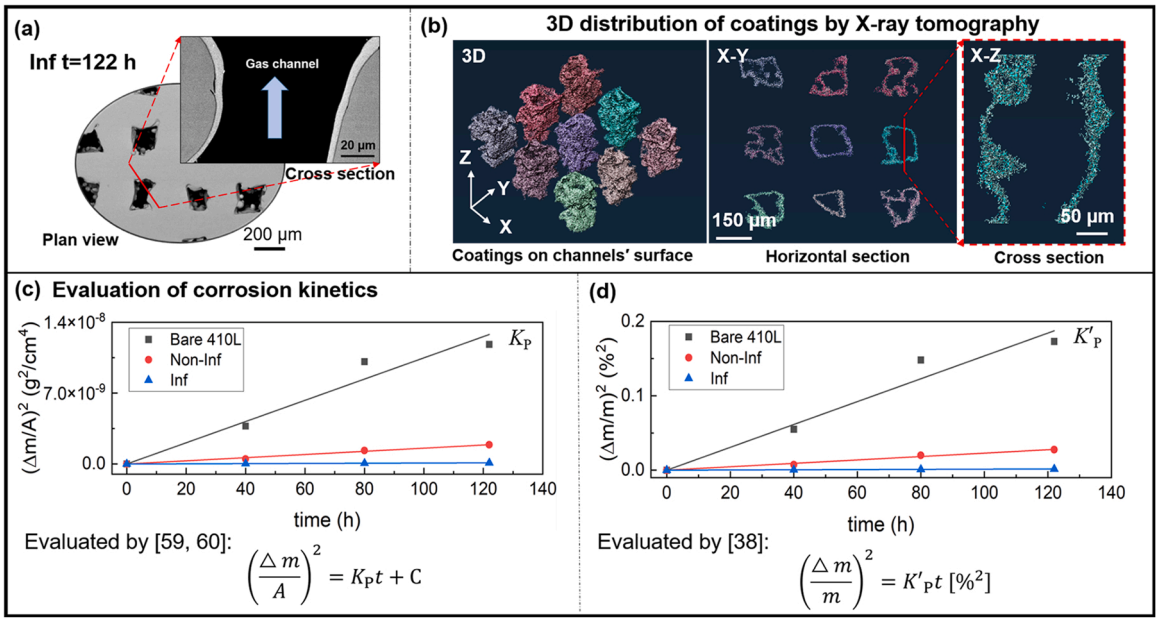

Fig. 10. Evaluation of multi-coated samples. (a) SEM images of after-test multi-coated sample in plan view and cross-section view; (b) 3D distribution of coatings by X-ray computed tomography; (c) and (d) are fitting results of the oxidation mass gain according to Eqs. (5) and (6), respectively.

Table 2
Summary of the anti-oxidation coating in this work and previous results.

Steel type (wt% Cr)	Structure	Coating	Fabrication/Coating method	Test conditions	K_P ($\times 10^{-15}$ $g^2cm^{-4}s^{-1}$)	K'_P ($\times 10^{-4}$ $\%^2$ h^{-1})	Ref/year
410L (12.5% Cr)	Porous (21.67%)	Bare	LPBF	Air-3% H_2O/750 ℃/122 h	29.09	15.4	This work
410L (12.5% Cr)	Porous (21.67%)	CGO	LPBF/EPD	Air-3% H_2O/750 ℃/122 h	4.34	2.29	This work
410L (12.5% Cr)	Porous (21.67%)	CGO/$Ce(NO_3)_3$	LPBF/EPD+Infiltration	Air-3% H_2O/750 ℃/122 h	0.26	0.14	This work
Höganäs ferritic alloy (20.6 % Cr)	Porous (30-35%)	$La(Mn,Co)_{0.8}O_3$	PM/Infiltration	Air/700 ℃/188.6 h	1.7	/	[8]/2020
Höganäs ferritic alloy (20.6 % Cr)	Porous (30-35%)	$La(Mn,Co)_{0.8}O_3$	PM/Infiltration	Ar-2.5%H_2O-5% H_2/700 ℃/212.9 h	0.056	/	[8]/2020
IN625 (20.1% Cr)	Porous (30%)	$Y(NO_3)_3$	PM/Infiltration	Air/700 ℃/500 h	/	1.46	[14]/2018
Crofer 22APU (23% Cr)	Dense	CGO	/EPD	H_2-90% H_2O/750 ℃/2000 h	3.45	/	[11]/2019
Crofer 22APU (23% Cr)	Dense	$MnCo_{1.7}Fe_{0.3}O_4$	/EPD	Air/800 ℃/5000 h	3.4	/	[44]/2017

Note K'_P of 1.46×10^{-4} $\%^2$ h^{-1} was calculated according to the data given in Fig. 1b of Ref. [14]. PM is powder metallurgy.

with a minimum error when the samples' porosity is at the same level. Compared with the bare 410 L metal support, coated samples Non-Inf and Inf show much smaller parabolic rate constants. The calculated values of K_P and K'_P are shown in Table 2 below.

Large K_P and K'_P are registered for the bare 410 L support after the ageing. An uneven oxide layer of ~2 μm thick, accompanied by exfoliating, was observed, as shown in Fig. S3 (supporting information). Taking K_P and K'_P of the bare 410 L support as the standard, an order of magnitude reduction is shown for 410 L support with CGO coating (Non-Inf sample), while two orders of magnitude reduction for the Inf sample. The active ceria-based multi-coatings allow low-cost 410 L stainless steel with 12.5 wt. % Cr to achieve acceptable corrosion resistance compared with other high-Cr stainless steel in Table 2. Moreover, the active ceria-based multi-coatings work simultaneously as the anti-oxidation layer and elemental diffusion barrier layer. This feature in SOCs is desirable as it avoids electrode elemental contamination.

4. Conclusions

We show that chemically active ceria-based multi-coatings improve the oxidation/corrosion resistance of 3D-printed metal support. LPBF fabricated 410 L stainless steel supports with regular-distributed vertical gas channels represent an optimized structure with a stable inner surface. The proposed metal support design allows the surface to be coated by a continuous CGO layer with nanopores using EPD. The following infiltration process greatly improved the ceramic coating and ceramic/steel interface in uniformity and density, mainly attributed to the fast mass diffusion-reaction interface and the filled CeO_2.

The combined action of physical and chemical protection mechanisms inhibits the oxide layer's growth and chromium evaporation. The formation of $Mn_{1-x}Fe_xCr_2O_4$ and the possible presence of $REMO_3$ oxides layer traps the migration of metal ions; on the other hand, humid air is restricted from contact with the oxide layer due to the coating's catalytic activity to H_2O and O_2 and its dense structure. The oxidation-resistant metal support showed excellent electro-chemo-mechanical stability with 3D active ceria-based multi-coatings, represented by a stable ASR and a record value of K_P of 0.26×10^{-15} g^2 cm^4 s^{-1} at 750 °C in air-3 % vol of H_2O.

CRediT authorship contribution statement

Zhipeng Zhou: Conceptualization, Methodology, Investigation, Formal analysis, and Writing-Original Draft; Venkata Karthik Nadimpalli: Investigation, Resources, Writing-Review & Editing, and Supervision; Aakil Raj Lalwani: Software and Investigation; Shu Wang: Investigation and Formal analysis; Yijing Shang: Software and Formal analysis; Zhihao Pan: Software and Formal analysis; David Bue Pedersen: Resources, Funding acquisition, and Supervision; Vincenzo Esposito: Conceptualization, Methodology, Formal analysis, Writing-Review & Editing, Supervision, and Project administration. All authors have read and agreed to the published version of the manuscript.

Declaration of Competing Interest

The authors declare that they have no known competing financial interests or personal relationships that could have appeared to influence the work reported in this paper.

Data Availability

Data will be made available on request.

Acknowledgements

We are indebted to DTU colleagues Ming Chen, Yun Xie, Carsten Grundlach, Sina Baier, Qingjie Wang, Jun Zhang, and Ebtisam Abdellahi for their valuable discussion and assistance with experiments and Achilles Bergne for the English proofreading. We gratefully acknowledge the financial support from China Scholarship Council (Grant No. 202006370033) and the Poul Due Jensen Foundation funding under the Open Additive Manufacturing Initiative grant.

Appendix A. Supporting information

Supplementary data associated with this article can be found in the online version at doi:10.1016/j.corsci.2023.111010.

References

[1] C. Zhao, Y. Li, W. Zhang, Y. Zheng, X. Lou, B. Yu, J. Chen, Y. Chen, M. Liu, J. Wang, Heterointerface engineering for enhancing the electrochemical performance of solid oxide cells, Energy Environ. Sci. 13 (1) (2020) 53–85, https://doi.org/10.1039/C9EE02230A.
[2] Z. Zhou, V.K. Nadimpalli, D.B. Pedersen, V. Esposito, Degradation mechanisms of metal-supported solid oxide cells and countermeasures: a review, Mater 14 (11) (2021) 3139, https://doi.org/10.3390/ma14113139.
[3] L. Barelli, G. Bidini, D.A. Ciupăgeanu, C. Pianese, P. Polverino, M. Sorrentino, Stochastic power management approach for a hybrid solid oxide fuel cell/battery auxiliary power unit for heavy duty vehicle applications, Energy Convers. Manag. 221 (2020), 113197, https://doi.org/10.1016/j.enconman.2020.113197.
[4] P. Satardekar, D. Montinaro, M.Z. Naik, V.M. Sglavo, Production of metal-supported solid oxide fuel cells by co-sintering route, Mater. Today.: Proc. 63 (2022) 76–84, https://doi.org/10.1016/j.matpr.2022.02.327.
[5] J.T.S. Irvine, P.S. Connor, Solid Oxide Fuels Cells: Facts and Figures, Spinger, London, UK, 2013.
[6] M.C. Tucker, Progress in metal-supported solid oxide fuel cells: a review, J. Power Sources 195 (15) (2010) 4570–4582, https://doi.org/10.1016/j.jpowsour.2010.02.035.
[7] E. Stefan, D. Neagu, P. Blennow Tullmar, Å.H. Persson, B.R. Sudireddy, D. Miller, M. Chen, J. Irvine, Spinel-based coatings for metal supported solid oxide fuel cells,

Mater. Res. Bull. 89 (2017) 232–244, https://doi.org/10.1016/j.materresbull.2017.02.003.
[8] E. Stefan, C. Denonville, Y. Larring, M. Stange, R. Haugsrud, Oxidation study of porous metal substrates for metal supported proton ceramic electrolyzer cells, Corros. Sci. 164 (2020), 108335, https://doi.org/10.1016/j.corsci.2019.108335.
[9] H. Jeong, D. Roehrens, M. Bram, Facile route for reactive coating of $LaCrO_3$ on high-chromium steels as protective layer for solid oxide fuel cell applications, Mater. Lett. 258 (2020), 126794, https://doi.org/10.1016/j.matlet.2019.126794.
[10] R. Knibbe, H.-J. Wang, P. Blennow, K. Thydén, Å.H. Persson, L. Mikkelsen, T. Klemensø, Oxidation in ceria infiltrated metal supported SOFCs – a TEM investigation, J. Power Sources 228 (2013) 75–82, https://doi.org/10.1016/j.jpowsour.2012.11.051.
[11] S. Molin, Å.H. Persson, T.L. Skafte, A.L. Smitshuysen, S.H. Jensen, K.B. Andersen, H. Xu, M. Chen, P.V. Hendriksen, Effective yttrium based coating for steel interconnects of solid oxide cells: corrosion evaluation in steam-hydrogen atmosphere, J. Power Sources 440 (2019), 226814, https://doi.org/10.1016/j.jpowsour.2019.226814.
[12] Y. Yan, R. Bateni, J. Harris, O. Kesler, Fabrication of reactive element oxide coatings on porous ferritic stainless steel for use in metal-supported solid oxide fuel cells, Surf. Coat. Technol. 272 (2015) 415–427, https://doi.org/10.1016/j.surfcoat.2015.03.041.
[13] S. Chevalier, P. Larpin, Formation of perovskite type phases during the high temperature oxidation of stainless steels coated with reactive element oxides, Acta Mater. 50 (2002) 3105–3114, https://doi.org/10.1016/S1359-6454(02)00106-4.
[14] J. Karczewski, K. Dunst, P. Jasinski, S. Molin, Influence of yttria surface modification on high temperature corrosion of porous Ni22Cr alloy, Int. J. Appl. Ceram. Technol. 15 (2) (2018) 361–369, https://doi.org/10.1111/ijac.12840.
[15] S. Hu, W. Li, H. Finklea, X. Liu, A review of electrophoretic deposition of metal oxides and its application in solid oxide fuel cells, Adv. Colloid Interface Sci. 276 (2020), 102102, https://doi.org/10.1016/j.cis.2020.102102.
[16] P. Nyamekye, P. Nieminen, M.R. Bilesan, E. Repo, H. Piili, A. Salminen, Prospects for laser based powder bed fusion in the manufacturing of metal electrodes: a review, Appl. Mater. Today 23 (2021), 101040, https://doi.org/10.1016/j.apmt.2021.101040.
[17] J.P. Oliveira, A.D. LaLonde, J. Ma, Processing parameters in laser powder bed fusion metal additive manufacturing, Mater. Des. 193 (2020), 108762, https://doi.org/10.1016/j.matdes.2020.108762.
[18] Q. Wei, H. Li, G. Liu, Y. He, Y. Wang, Y.E. Tan, D. Wang, X. Peng, G. Yang, N. Tsubaki, Metal 3D printing technology for functional integration of catalytic system, Nat. Commun. 11 (1) (2020) 4098, https://doi.org/10.1038/s41467-020-17941-8.
[19] L. Yang, C. Yan, W. Cao, Z. Liu, B. Song, S. Wen, C. Zhang, Y. Shi, S. Yang, Compression–compression fatigue behaviour of gyroid-type triply periodic minimal surface porous structures fabricated by selective laser melting, Acta Mater. 181 (2019) 49–66, https://doi.org/10.1016/j.actamat.2019.09.042.
[20] J. Nielsen, Å.H. Persson, T.T. Muhl, K. Brodersen, Towards high power density metal supported solid oxide fuel cell for mobile applications, J. Electrochem. Soc. 165 (2) (2018) F90–F96, https://doi.org/10.1149/2.0741802jes.
[21] F. Teocoli, D.W. Ni, S. Sanna, K. Thydén, F.C. Fonseca, V. Esposito, Fast mass interdiffusion in ceria/alumina composite, J. Mater. Chem. A 3 (33) (2015) 17135–17143, https://doi.org/10.1039/c5ta02416a.
[22] M. Cargnello, V.T. Doan-Nguyen Vicky, R. Gordon Thomas, E. Diaz Rosa, A. Stach Eric, J. Gorte Raymond, P. Fornasiero, B. Murray Christopher, Control of metal nanocrystal size reveals metal-support interface role for ceria catalysts, Science 341 (6147) (2013) 771–773, https://doi.org/10.1126/science.1240148.
[23] Y. Wang, C. Cui, Y. Tong, S. Wang, R. Peng, C. Chen, Z. Zhan, Dopant-induced surface activation of ceria nanorods for electro-oxidation of hydrogen and propane in solid oxide fuel cells, Int. J. Hydrog. Energy 46 (34) (2021) 17922–17931, https://doi.org/10.1016/j.ijhydene.2021.02.193.
[24] M. Biesuz, G. Dell'Agli, L. Spiridigliozzi, C. Ferone, V.M. Sglavo, Conventional and field-assisted sintering of nanosized Gd-doped ceria synthesized by co-precipitation, Ceram. Int. 42 (10) (2016) 11766–11771, https://doi.org/10.1016/j.ceramint.2016.04.097.
[25] N. Mahato, A. Banerjee, A. Gupta, S. Omar, K. Balani, Progress in material selection for solid oxide fuel cell technology: a review, Prog. Mater. Sci. 72 (2015) 141–337, https://doi.org/10.1016/j.pmatsci.2015.01.001.
[26] M. Bianco, M. Linder, Y. Larring, F. Greco, J. Van herle, Lifetime issues for solid oxide fuel cell interconnects. Solid Oxide Fuel Cell Lifetime and Reliability, Elsevier, Amsterdam, The Netherlands, 2017, pp. 121–144.
[27] M.C. Tucker, Progress in metal-supported solid oxide electrolysis cells: a review, Int. J. Hydrog. Energy 45 (46) (2020) 24203–24218, https://doi.org/10.1016/j.ijhydene.2020.06.300.
[28] V. Esposito, D.W. Ni, Z. He, W. Zhang, A.S. Prasad, J.A. Glasscock, C. Chatzichristodoulou, S. Ramousse, A. Kaiser, Enhanced mass diffusion phenomena in highly defective doped ceria, Acta Mater. 61 (16) (2013) 6290–6300, https://doi.org/10.1016/j.actamat.2013.07.012.
[29] V. Esposito, D.W. Ni, D. Marani, F. Teocoli, K.T. Sune Thydén, D.Z. De Florio, F. C. Fonseca, Accelerated ceria–zirconia solubilization by cationic diffusion inversion at low oxygen activity, J. Mater. Chem. A 4 (43) (2016) 16871–16878, https://doi.org/10.1039/C6TA06308J.
[30] D.W. Ni, J.A. Glasscock, A. Pons, W. Zhang, A. Prasad, S. Sanna, N. Pryds, V. Esposito, Densification of highly defective ceria by high temperature controlled re-oxidation, J. Electrochem. Soc. 161 (11) (2014) F3072–F3078, https://doi.org/10.1149/2.0121411jes.
[31] F. Teocoli, V. Esposito, Viscoelastic properties of doped-ceria under reduced oxygen partial pressure, Scr. Mater. 75 (2014) 82–85, https://doi.org/10.1016/j.scriptamat.2013.11.027.
[32] S.A. Andersen, D. Pedersen, H. Hansen, J. Spangenberg, J. Taylor, N. Kjelgaard Vedel-Smith, Open Architecture Laser Power Bed Additive Manufacturing, 2020.
[33] M. Ahmadi, H. Aghajani, Suspension characterization and electrophoretic deposition of Yttria-stabilized Zirconia nanoparticles on an iron-nickel based superalloy, Ceram. Int. 43 (9) (2017) 7321–7328, https://doi.org/10.1016/j.ceramint.2017.03.035.
[34] F. Chen, M. Liu, Preparation of yttria-stabilized zirconia (YSZ) films on $La_{0.85}Sr_{0.15}MnO_3$ (LSM) and LSM±YSZ substrates using an electrophoretic deposition (EPD) process, J. Eur. Ceram. Soc. 21 (2001) 127–134, https://doi.org/10.1016/S0955-2219(00)00195-3.
[35] D. Wang, L. Liu, G. Deng, C. Deng, Y. Bai, Y. Yang, W. Wu, J. Chen, Y. Liu, Y. Wang, X. Lin, C. Han, Recent progress on additive manufacturing of multi-material structures with laser powder bed fusion, Virtual Phys. Prototyp. 17 (2) (2022) 329–365, https://doi.org/10.1080/17452759.2022.2028343.
[36] D.W. Ni, V. Esposito, Densification of $Ce_{0.9}Gd_{0.1}O_{1.95}$ barrier layer by in-situ solid state reaction, J. Power Sources 266 (2014) 393–400, https://doi.org/10.1016/j.jpowsour.2014.05.044.
[37] Z. Yang, G. Xia, P. Singh, J.W. Stevenson, Effects of water vapor on oxidation behavior of ferritic stainless steels under solid oxide fuel cell interconnect exposure conditions, Solid State Ion. 176 (17) (2005) 1495–1503, https://doi.org/10.1016/j.ssi.2005.03.019.
[38] S. Molin, B. Kusz, M. Gazda, P. Jasinski, Evaluation of porous 430L stainless steel for SOFC operation at intermediate temperatures, J. Power Sources 181 (1) (2008) 31–37, https://doi.org/10.1016/j.jpowsour.2007.10.009.
[39] C. Jia, Y. Wang, S. Molin, Y. Zhang, M. Chen, M. Han, High temperature oxidation behavior of SUS430 SOFC interconnects with Mn-Co spinel coating in air, J. Alloy. Compd. 787 (2019) 1327–1335, https://doi.org/10.1016/j.jallcom.2019.01.015.
[40] S. Molin, M. Gazda, B. Kusz, P. Jasinski, Net shape processed electrolyte on 316L porous metal supported SOFC, Eur. Ceram. Soc. (2008).
[41] S. Cui, Y. Liu, T. Wang, K. Tieu, L. Wang, D. Zeng, Z. Li, W. Li, Tribological behavior comparisons of high chromium stainless and mild steels against high-speed steel and ceramics at high temperatures, Friction 10 (3) (2021) 436–453, https://doi.org/10.1007/s40544-021-0509-1.
[42] X. Cheng, Z. Jiang, D. Wei, J. Zhao, B.J. Monaghan, R.J. Longbottom, L. Jiang, High temperature oxidation behaviour of ferritic stainless steel SUS 430 in humid air, Met. Mater. Int. 21 (2) (2015) 251–259, https://doi.org/10.1007/s12540-015-4168-5.
[43] J.C.W. Mah, A. Muchtar, M.R. Somalu, M.J. Ghazali, Metallic interconnects for solid oxide fuel cell: a review on protective coating and deposition techniques, Int. J. Hydrog. Energy 42 (14) (2017) 9219–9229, https://doi.org/10.1016/j.ijhydene.2016.03.195.
[44] B. Talic, H. Falk-Windisch, V. Venkatachalam, P.V. Hendriksen, K. Wiik, H.L. Lein, Effect of coating density on oxidation resistance and Cr vaporization from solid oxide fuel cell interconnects, J. Power Sources 354 (2017) 57–67, https://doi.org/10.1016/j.jpowsour.2017.04.023.
[45] T. Akashi, M. Nanko, T. Maruyama, Y. Shiraishi, J. Tanabe, Solid-state reaction kinetics of $LaCrO_3$ from the oxides and determination of La^{3+} diffusion coefficient, J. Electrochem. Soc. 145 (6) (1998) 2090–2094, https://doi.org/10.1149/1.1838601.
[46] T.A. Ramanarayanan, J.D. Mumford, C.M. Chun, R.A. Petkovic, Transport through chromia films, Solid State Ion. 136-137 (2000) 83–90, https://doi.org/10.1016/S0167-2738(00)00355-6.
[47] L. Mikkelsen, High temperature oxidation of iron-chromium alloys. Ph.D. Thesis, Risø National Laboratory, Roskilde, Denmark, 2003.
[48] S. Kumar, D. Mudgal, S. Singh, S. Prakash, Effect of CeO_2 in Cr_3C_2-NiCr coating on Superni 600 at high temperature, Procedia Mater. Sci. 6 (2014) 939–949, https://doi.org/10.1016/j.mspro.2014.07.164.
[49] S. Roure, F. Czerwinsk, A. Petric, Influence of CeO_2-coating on the high-temperature oxidation of chromium, Oxid. Met. 42 (1994) 75–102, https://doi.org/10.1007/BF01061925.
[50] D.H. Peck, M. Miller, D. Kobertz, H. Nickel, K. Hilpert, Vaporization of $LaCrO_3$: partial and integral thermodynamic properties, J. Am. Ceram. Soc. 79 (12) (1996) 3266–3272, https://doi.org/10.1111/j.1151-2916.1996.tb08104.x.
[51] F. Ye, H. Dai, M. Wang, J. Chen, T. Li, Z. Chen, The structural, dielectric, and magnetic properties of $GdMnO_3$ multiferroic ceramics, J. Mater. Sci.: Mater. Electron. 31 (4) (2020) 3590–3597, https://doi.org/10.1007/s10854-020-02909-7.
[52] L. Zhou, Z. Zeng, M.P. Brady, D.N. Leonard, H.M. Meyer, Y. Yamamoto, W. Li, G. Collins, X. Liu, Chromium evaporation and oxidation characteristics of alumina-forming austenitic stainless steels for balance of plant applications in solid oxide fuel cells, Int. J. Hydrog. Energy 46 (41) (2021) 21619–21633, https://doi.org/10.1016/j.ijhydene.2021.04.002.

[53] J.I. Goldstein, D.E. Newbury, J.R. Michael, N.W.M. Ritchie, J.H.J. Scott, D.C. Joy, Scanning Electron Microscopy and X-Ray Microanalysis, Springer, New York, 2017, https://doi.org/10.1007/978-1-4939-6676-9.
[54] L. Hou, L. Shi, J. Zhao, S. Zhou, S. Pan, X. Yuan, Y. Xin, Room-temperature multiferroicity in CeFeO3 ceramics, J. Alloy. Compd. 797 (2019) 363–369, https://doi.org/10.1016/j.jallcom.2019.05.078.
[55] Y. Cao, J. Liang, X. Li, L. Yue, Q. Liu, S. Lu, A.M. Asiri, J. Hu, Y. Luo, X. Sun, Recent advances in perovskite oxides as electrode materials for supercapacitors, Chem. Commun. (Camb.) 57 (19) (2021) 2343–2355, https://doi.org/10.1039/d0cc07970g.
[56] R. Wang, C. Byrne, M.C. Tucker, Assessment of co-sintering as a fabrication approach for metal-supported proton-conducting solid oxide cells, Solid State Ion. 332 (2019) 25–33, https://doi.org/10.1016/j.ssi.2019.01.004.
[57] F. Sadi, Hydrogen formation in the reaction of steam with Rh/CeO_2 catalysts: a tool for characterising reduced centres of ceria, J. Catal. 213 (2) (2003) 226–234, https://doi.org/10.1016/s0021-9517(02)00080-5.
[58] A. Trovarelli, M. Boaro, E. Rocchini, C. de Leitenburg, G. Dolcetti, Some recent developments in the characterization of ceria-based catalysts, J. Alloy. Compd. 323–324 (2001) 584–591, https://doi.org/10.1016/S0925-8388(01)01181-1.
[59] K. Przybylski, T. Brylewski, E. Durda, R. Gawel, A. Kruk, Oxidation properties of the Crofer 22 APU steel coated with $La_{0.6}Sr_{0.4}Co_{0.2}Fe_{0.8}O_3$ for IT-SOFC interconnect applications, J. Therm. Anal. Calor. 116 (2) (2014) 825–834, https://doi.org/10.1007/s10973-013-3594-1.
[60] S. Mrowec, T. Werber. Modern scaling-resistant materials, National of Standards and National Science Foundation, Washington DC, 1982.